metals

MDPI

Article

Characterization of Various Stainless Steels Containing Gadolinium as Thermal Neutron Absorbing and Shielding Materials

SeKwon Oh [1], Ji-Ho Ahn [1], Rockhoon Jung [2], Hyun-Jong Kim [1], Younghwan Chu [3], Dae Hyun Choi [4], Hyun Lee [5,6] and Hyun-Do Jung [5,6,*]

[1] Research Institute of Advanced Manufacturing Technology, Korea Institute of Industrial Technology, Incheon 21999, Republic of Korea; sk0514@kitech.re.kr (S.O.); dkswlgh8@kitech.re.kr (J.-H.A.); hjkim23@kitech.re.kr (H.-J.K.)
[2] Ship & Offshore Research Institute, Samsung Heavy Industries, Pangyo R&D Center, Seongnam-si 13486, Republic of Korea; rhoon.jung@samsung.com
[3] Fospia Co., Ltd., Mado-ro, Mado-myeon, Hwaseong-si 18541, Republic of Korea; crystal@fospia.com
[4] SHINWOO CNC KOREA Co., LTD, 87, Gongdan-ro, Goseong-eup, Goseong-gun 52948, Republic of Korea; ch240ch240@gmail.com
[5] Department of Biomedical-Chemical Engineering, The Catholic University of Korea, Bucheon 14662, Republic of Korea; leeh0520@catholic.ac.kr
[6] Department of Biotechnology, The Catholic University of Korea, Bucheon 14662, Republic of Korea
* Correspondence: hdjung@catholic.ac.kr; Tel.: +82-2-2164-4357

Abstract: Developing next-generation thermal-neutron-shielding and -absorbing materials for the safe storage and transportation of spent nuclear fuel is a topic of active research in academia. Gadolinium (Gd) boasts superior neutron absorption capacity compared with other nuclei. Consequently, it has garnered significant attention as a potential replacement for boron in spent nuclear fuel (SNF) applications. In this study, the austenitic stainless steels 304 and 316 and the duplex stainless steel 5A were reinforced with 2 wt.% of gadolinium to explore their thermal-neutron-absorbing efficiency. Their properties were then compared with commercial-grade borated stainless steel, as per ASTM standard A887. After the inclusion of Gd, both the yield strength and ultimate tensile strength of the alloys slightly increased, which was attributed to the evenly distributed Gd intermetallics within the matrix. However, the elongation rate was reduced. The Charpy impact absorption energy also decreased. The influence of the Gd intermetallic was further explored by examining the fractography. While the corrosion resistance of the alloy slightly diminished after the addition of Gd, its neutron absorption capacity demonstrated superior performance, especially when the Gd content was equivalent to that of boron. Although most properties of the experimental alloy deteriorated after the Gd addition, they still outperformed commercial borated stainless steel, suggesting that this alloy might be a promising candidate for SNF applications.

Keywords: gadolinium; stainless steel; neutron-absorbing material; mechanical properties; microstructure; corrosion resistance

Citation: Oh, S.; Ahn, J.-H.; Jung, R.; Kim, H.-J.; Chu, Y.; Choi, D.H.; Lee, H.; Jung, H.-D. Characterization of Various Stainless Steels Containing Gadolinium as Thermal Neutron Absorbing and Shielding Materials. *Metals* **2024**, *14*, 16. https://doi.org/10.3390/met14010016

Academic Editors: Shilong Liu and Xiucheng Li

Received: 4 December 2023
Revised: 17 December 2023
Accepted: 20 December 2023
Published: 22 December 2023

1. Introduction

Spent nuclear fuel (SNF) generated by nuclear reactors has the inherent capability to undergo spontaneous fission, resulting in the emission of intense neutrons and gamma rays [1–4]. These emissions pose significant radiation risks to both individuals and the surrounding environment, necessitating careful and proper disposal. The safe management of SNF hinges on effective transportation and storage practices, with neutron-shielding and -absorbing materials serving as pivotal components [5,6].

Among these materials, boron steel and boron carbide (B_4C)/aluminum (Al) composite materials are notable examples, where they rely on the high thermal neutron absorption

cross-section of boron-10 (^{10}B) [7]. These materials find application in the storage racks and transport casks used for SNF. To enhance the neutron-shielding and -absorbing effectiveness of boron steel, enriched ^{10}B is typically introduced into steel through alloying. This process, however, is intricate and costly. Moreover, the highest achievable boron (B) content in such steel remains limited to 2.25 wt% [8]. Unfortunately, boron steel with this B content cannot entirely shield thermal neutrons, and its mechanical properties significantly deteriorate beyond this concentration [4]. Consequently, it is deemed unsuitable for the secure transportation and storage of SNF. Furthermore, the borides within boron steel tend to form helium bubbles upon neutron absorption, leading to the degradation of shielding materials over extended storage periods, thereby posing safety risks [9].

On the other hand, B_4C/Al neutron-shielding materials can contain substantially higher B_4C content, up to 35 wt%. However, materials with such elevated B_4C content exhibit exceptional hardness, making them challenging to process and shape [10]. Additionally, B_4C/Al composites as thermal-neutron-absorbing and -shielding materials cannot function as standalone structural materials and require a boron steel cladding layer for structural support. This complex design results in containers with intricate structures and limited storage capacity, rendering them inconvenient for use, cleaning, and maintenance [11]. Evidently, there exists a trade-off between the content of neutron-absorbing elements and the properties of neutron-absorbing and -shielding materials.

Gadolinium (^{155,157}Gd) boasts the highest thermal neutron absorption cross-section value compared with other nuclei. Furthermore, when considering thermal neutron cross-section values, ^{157}Gd boasts an exceptional advantage, presenting an approximately 60-fold increase (240,000 b) compared with boron (^{10}B) (3810 b) [12]. At an equivalent content, Gd exhibits a thermal neutron absorption capacity more than four times greater than that of ^{10}B, and it comes at a significantly reduced cost, ranging from 1/12 to 1/5 of ^{10}B [13]. Furthermore, Gd effectively mitigates helium bubble formation during neutron absorption reactions, thus extending the service life of neutron-absorbing and -shielding materials [14]. Substituting Gd for B in the production of thermal-neutron-absorbing and -shielding materials presents a solution to the content–performance dilemma. This approach allows for achieving superior neutron-shielding rates and enhanced material properties with lower Gd content.

Stainless steels (SSs) and nickel-based alloys are well regarded for their formidable mechanical strength and robust corrosion resistance. As a result, there has been considerable exploration into the amalgamation of Gd with various materials, including nickel-based alloys [15,16], austenitic stainless steels [17–19], and duplex stainless steels (DSSs) [20,21]. These alloys demonstrate promise in terms of reactivity control and structural functionality, albeit at the expense of reduced toughness and ductility owing to the formation of Gd-rich precipitated intermetallics. In recent developments, there has been growing interest in novel alloys that incorporate both Gd isotopes, aiming to strike a balance between effective neutron absorption and structural integrity [22,23].

SS 304, SS 316, and ASTM A890 5A grade duplex stainless steel were selected as base materials. To introduce Gd, 2 wt. % was incorporated and the alloys were prepared using vacuum arc melting (VAM). For a detailed examination of the alloy microstructures and inclusions, a field-emission scanning electron microscope (FE-SEM) was employed. The phases and compositions of these alloys were determined using X-ray diffraction (XRD) and energy-dispersive X-ray spectroscopy (EDS). Furthermore, the mechanical properties were assessed using tensile and Charpy impact resistance testing, while the corrosion resistance was evaluated via electrochemical corrosion tests.

2. Experimental Procedures

2.1. Alloy Design and Production

The experimental alloys were fabricated with VAM using electrolytic iron (Fe), chromium (Cr), nickel (Ni), manganese (Mn), silicon (Si), ferro-molybdenum (Fe-60 wt%Mo), and ferrochromium nitride (Fe-60 wt%Cr-10 wt%N), and high-purity Gd (99.99%, Treibacher

Industrie AG, Hamburg, Germany). To prevent oxidation, the dissolution was conducted in a high-vacuum state of $\geq 1 \times 10^{-5}$ Torr and Argon (Ar) was used as the atmosphere gas of the chamber. In the case of the experimental alloy, remelting was performed five times by inverting each specimen up and down to prevent segregation and promote the uniform distribution of Gd.

In this study, SUS 304, SUS 316, and DSS 5A alloys (listed in ASTM standard A890) were selected as base materials and chemical compositions of the experimental alloys were analyzed using inductively coupled plasma optical emission spectroscopy (ICP-OES, iCAP-6300, Thermo Scientific, Amberg, Germany), and the results are shown in Table 1. The amount of Gd added was 2 wt.%, and the material property changes before and after the Gd addition were analyzed according to the amount of added Gd. Before the preparation of the experimental alloy, the solidification behavior was confirmed and the appropriate heat treatment temperature was determined using our previous studies.

Table 1. Chemical composition of the experimental alloys (wt.%).

Alloys	Fe	Cr	Ni	Mo	Mn	Si	N	Gd
304 (Aimed)	Bal.	18	10	-	1.3	0.8	0.1	2
304	Bal.	18.4	9.21	-	1.01	0.45	0.13	-
304-Gd	Bal.	18.1	9.44	-	1.13	0.62	0.12	1.76
316 (Aimed)	Bal.	18	12	2.4	1.3	0.8	0.1	2
316	Bal.	19.3	11.6	1.9	1.4	0.91	0.12	-
316-Gd	Bal.	18.3	10.9	2.12	1.19	0.77	0.14	2.13
5A (Aimed)	Bal.	25	7	4.5	1.3	0.8	0.3	2
5A	Bal.	25.4	7.17	4.23	1.16	0.65	0.25	-
5A-Gd	Bal.	25.8	7.63	4.34	1.22	0.78	0.28	1.96

The prepared experimental alloy was subjected to a solution heat treatment to remove the intermetallic compounds generated during solidification. In the case of 304 and 316 alloys, the solution heat treatment was performed at 1080 °C, and in the case of 5A, a solid solution heat treatment was performed at 1130 °C to create a ratio of α to γ phases equal to 45:55.

The evaluation of the neutron-absorbing capacity of the fabricated alloys in this study followed a previously established method [1]. In essence, we employed the Beer–Lambert Law to theoretically calculate the neutron transmission ratio, as expressed below [24]:

$$I/I_0 = e^{-N\sigma t} \quad (1)$$

Here, I_0 and I represent the neutron transmission intensity before and after passing through the absorber, respectively. N denotes the atom density, σ signifies the total cross-section, and t stands for the thickness of the neutron absorber. To determine the atom density (N) of each element (x), we used the following formula [1]:

$$N_x = \rho N_a n_x / M \quad (2)$$

where ρ represents the density of the compound, M stands for the molecular weight of the compound, N_a corresponds to Avogadro's number (6.022×10^{23} atoms/mol), and n_x indicates the number of atoms of element x within one compound. Table S1 shows the various parameters of Fe and Gd used to calculate the neutron transmission ratio. Since the neutron cross-section value of Gd is much higher compared with that of other elements composing steel, we performed the calculation using only Fe, which is the main component of steel, and Gd.

2.2. Microstructure Characterization

For the microstructural examinations, the experimental samples underwent a preparation process involving grinding with SiC sandpaper ranging from ~180 to 2000 grit, followed by polishing with diamond suspension slurries. The assessment of the experimental alloys, both with and without Gd, was conducted using the backscattered electron (BSE) mode of a Quanta 200 F field-emission scanning electron microscope (FE-SEM) from the FEI Company in the USA, both before and after the solution treatment. An energy-dispersive X-ray spectroscopy (EDS) attachment integrated with the FE-SEM was employed to analyze the elemental composition of the specimens. To characterize the alloy phases, X-ray diffraction (XRD) analysis was performed using a D8-discover instrument from Bruker in Germany with monochromatic Cu Kα radiation. The scanning spanned a diffraction angle range from 20° to 80°, operating at a rate of 1°/min. The α phase content was quantified employing a feritscope (FMP-30) manufactured by Fischer in Germany, boasting a remarkable α detection limit of 0.1%. Notably, each specimen was subjected to analysis across an average of 30 fields. Furthermore, the average sizes and areas of inclusions present in the alloys were assessed through the utilization of an inclusion analyzer (CTR 6000) produced by Leica in Berlin, Germany.

2.3. Mechanical Properties of the Experimental Alloys

To investigate the mechanical characteristics of the experimental alloys, including those with and without Gd, we conducted assessments of their tensile strength and Charpy impact resistance. Cylindrical specimens were subjected to elongation at a constant crosshead speed of 1 mm/min, following the guidelines outlined in the ASTM standard A370. This evaluation of tensile properties was carried out using an AGX 300KN testing machine manufactured by Shimadzu in Japan. Furthermore, Charpy impact tests, in accordance with the KS-0809 standard, were performed on V-notched specimens measuring $10 \times 10 \times 55$ mm^3. These tests were executed using a Charpy-type impact tester (SAID3) from Satec in the USA, all of which were conducted at a temperature of 25 °C. Subsequently, the fractured surfaces of the specimens following these tests were meticulously examined using an FE-SEM. To ensure the reliability of our findings, each mechanical test was conducted on more than five specimens for each alloy, allowing us to derive statistically significant outcomes. All quantitative data are presented as mean values accompanied by standard deviations. For the purpose of the statistical analysis, a one-way ANOVA was employed, with a significance threshold set at $p < 0.05$.

2.4. Electrochemical Corrosion Test

To assess the corrosion resistance of our experimental alloys immersed in artificial seawater, we employed an electrochemical potentiostat (VersaSTAT 3, AMETEK Scientific Instruments, Princeton, NJ, USA). The composition of the artificial seawater strictly adhered to the ASTM standard D1141–98, and its pH was adjusted to 8.2 for consistency.

For all electrochemical corrosion assessments, a conventional three-electrode cell setup was used, which featured a working electrode with a surface area of 1 cm^2, a platinum plate as the counter electrode, and an Ag/AgCl electrode functioning as the reference electrode. To ensure stability, each alloy sample was initially submerged in the artificial seawater for 30 min to achieve a steady open-circuit potential before the polarization scan commenced. Subsequently, we conducted a potential sweep ranging from −1000 to 1000 mV, operating at a scan rate of 0.1 mV/s. From the resulting potentiodynamic polarization curves, we calculated key parameters, such as the corrosion potential (Ecorr), corrosion current density (Icorr), and cathodic (βc) and anodic (βa) Tafel slopes. Additionally, the polarization resistance (Rp), which is essential for determining corrosion rates, was determined using the Stern–Geary equation [25]:

$$R_p = \frac{\beta_c \times \beta_a}{2.3 I_{corr}(\beta_c + \beta_a)} \quad (3)$$

3. Results and Discussion

3.1. Microstructural Characterization

All alloying elements, including Gd, were close to their target compositions. The 304, 304-Gd, 316, and 316-Gd alloys were heat treated at 1080 °C and the 5A and 5A-Gd alloys were treated at 1130 °C to remove intermetallic precipitates, such as σ phase compounds on the α, and obtain the ideal phase fraction. We tried to qualitatively analyze the phases of the experimental alloys using XRD analysis, and the results measured after the solution heat treatment are shown in Figure 1. In the case of the experimental alloys to which Gd was not added, no specific peak was observed and typical peaks of austenitic and DSS were observed. In the case of the 5A experimental alloy, the sigma (σ) phase and chi (χ) peaks, which are harmful intermetallic compounds, did not appear. In the cases of 304-Gd and 316-Gd, Gd-related peaks did not appear.

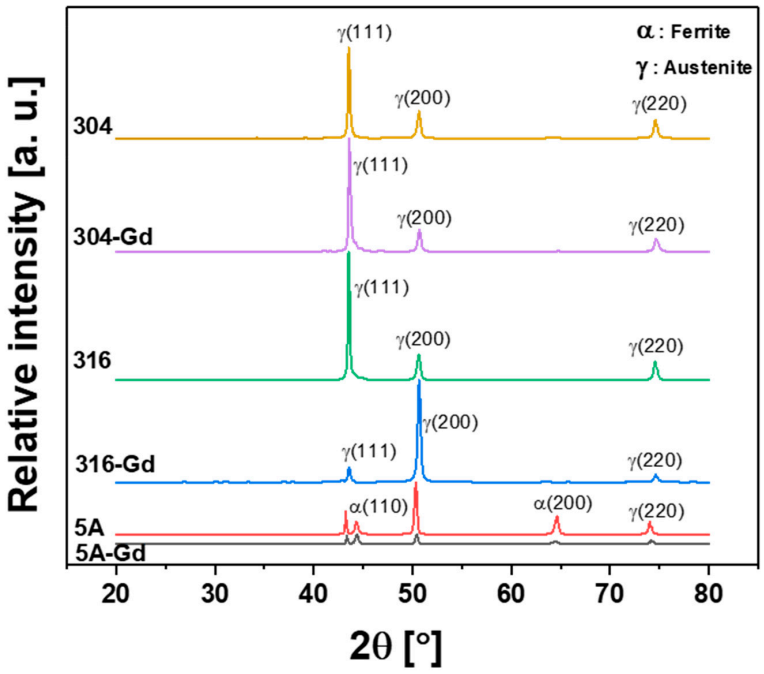

Figure 1. X-ray diffraction patterns of the experimental alloys after solution heat treatment.

Figure 2 shows SEM-BSE images after the solution heat treatment of 304-Gd, 316-Gd, and 5A-Gd. No microcracks or defects were found in any of the experimental alloys. The Gd intermetallic compounds showed a randomly distributed appearance throughout the specimen rather than a fixed appearance in a characteristic region or location. Also, no segregation or clusters were observed; there were no coarse intermetallic compounds. Because the experimental alloys were fabricated in a high vacuum, near 1×10^{-5} Torr, there were almost no oxides or inclusions. The composition of Gd intermetallics deposited in the experimental alloy was analyzed using SEM-EDS, and the results are shown in Figure 3. Most Gd intermetallics had a composition of Fe–Cr–Ni–Gd or Fe–Cr–Gd–N.

3.2. Mechanical Properties

The influence of Gd addition on the mechanical properties of the experimental alloys was examined by conducting tensile and Charpy impact tests. Figure 4 and Table 2 show the tensile test results. 5A showed higher tensile strength than 304 and 316 because it had a structure in which the α and γ phases were properly mixed. The ultimate tensile strength of 5A was 734 MPa, which was higher than that of the 304 and 316 alloys. The ultimate tensile strengths of 304-Gd, 316-Gd, and 5A-Gd were slightly increased compared with those of the alloys without Gd. The ultimate tensile strength of 304-Gd showed an improvement of approximately 7%, from 534 to 572.6 MPa, with Gd addition. The observed

improvement was by approximately 11%, from 455 to 503 MPa, in the 316-Gd. The ultimate tensile strength of 5A-Gd was 776 MPa, which was an improvement of approximately 6% with the addition of Gd.

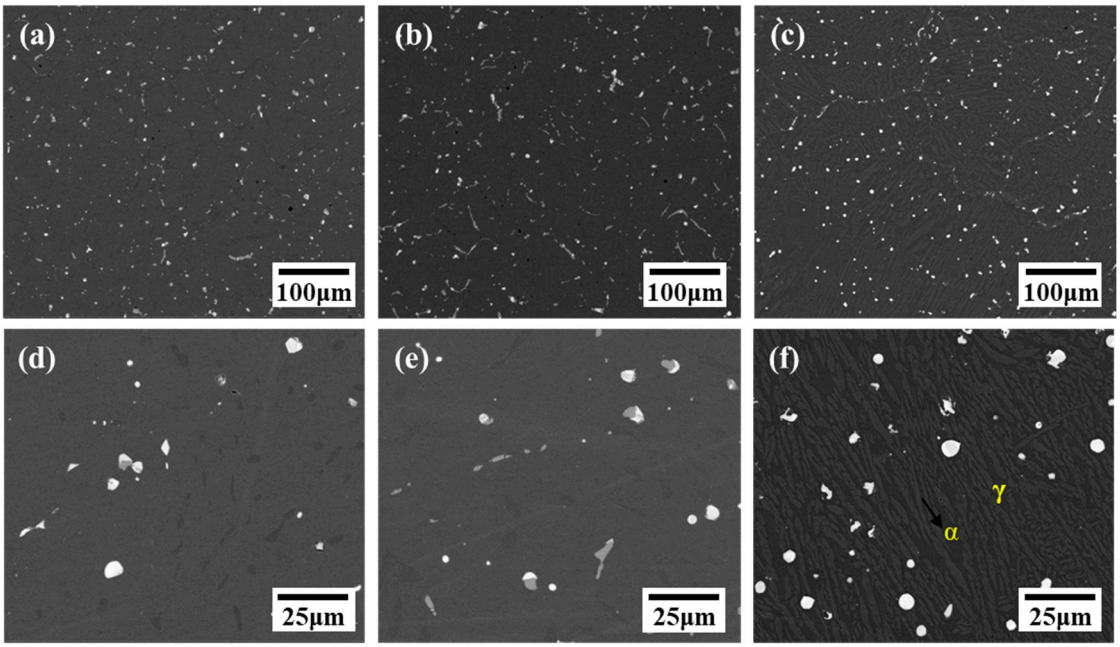

Figure 2. Representative backscattered electron (BSE) images of (**a**,**d**) 304-Gd, (**b**,**e**) 316-Gd, and (**c**,**f**) 5A-Gd. Upper images are low magnification and the lower images are high magnification.

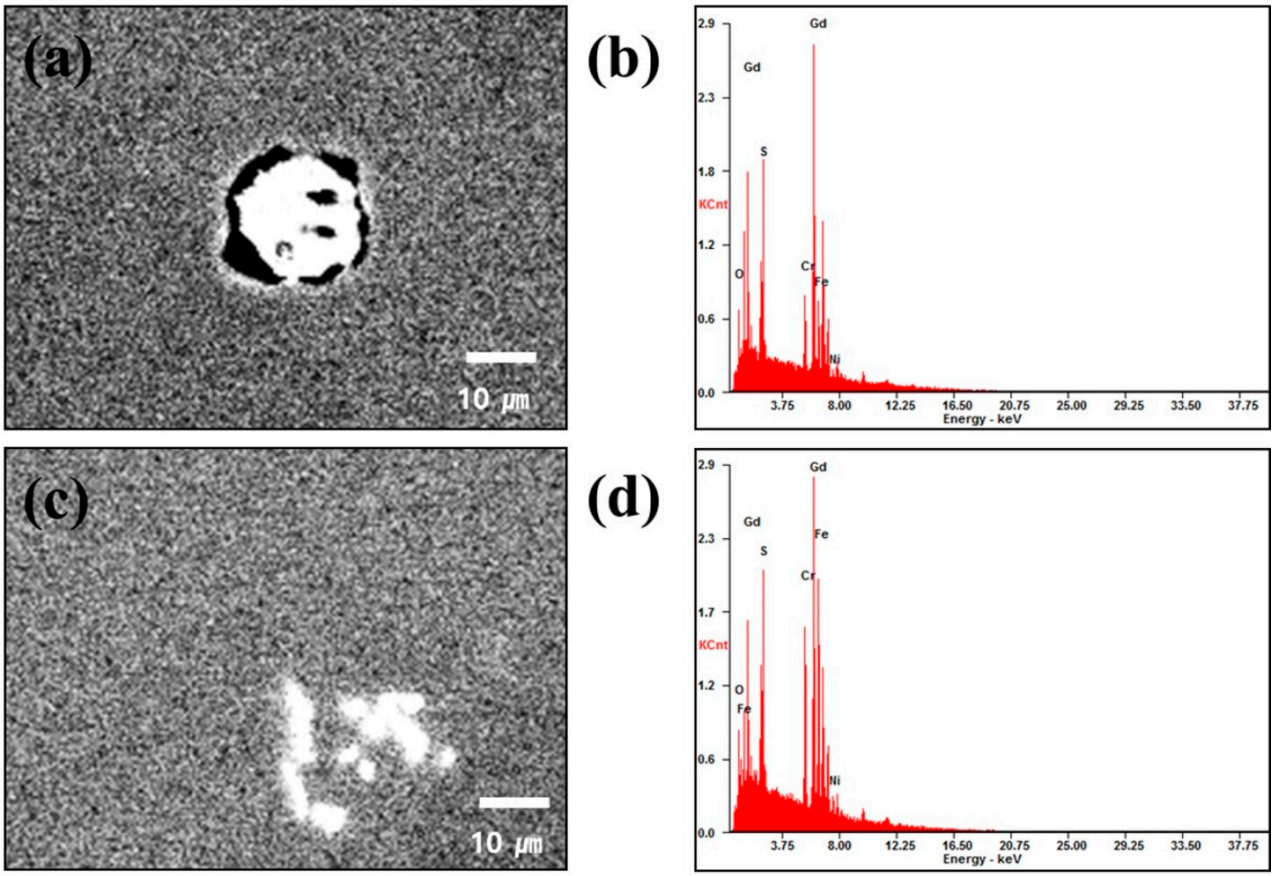

Figure 3. Representative (**a**,**c**) SEM images and (**b**,**d**) their EDS results of Gd-based intermetallics.

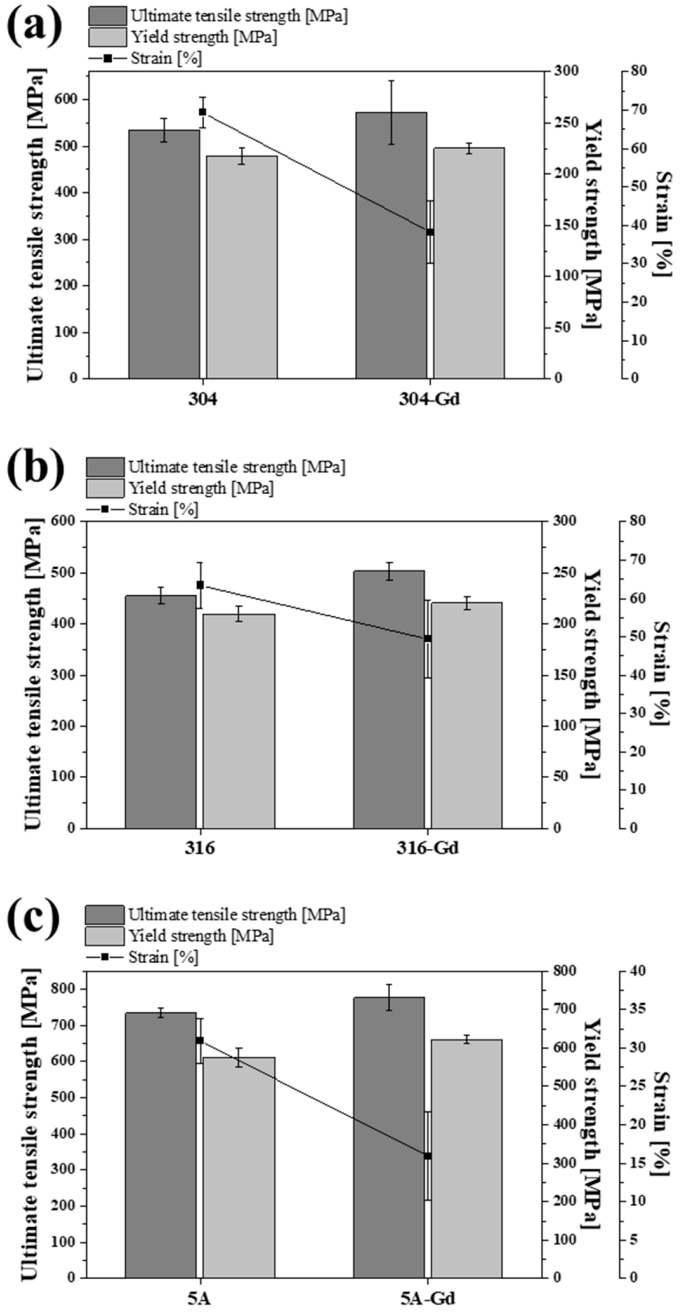

Figure 4. Changes in tensile properties of the experimental alloys with the addition of Gd: (**a**) 304 and 304-Gd, (**b**) 316 and 316-Gd, and (**c**) 5A and 5A-Gd.

The yield strength also slightly increased after Gd was added to the steels. In the case of 304, the yield strength was improved by approximately 4%, from 217 to 225 MPa. In the cases of 316 and 5A, yield strength improved by approximately 5%, from 209 to 220 MPa, and by approximately 8%, from 576 to 622 MPa, respectively. The improvements in ultimate tensile strength and yield strength are thought to be the result of the uniform distribution of Gd intermetallics generated by Gd addition to the matrix.

Conversely, the elongation of the Gd-added steels decreased significantly. In the case of 304, an approximately 44% decrease, from 69% to 38%, was observed after the addition of Gd. In the cases of 316 and 5A, the elongation decreased by approximately 22%, from 63% to 49%, and 48%, from 30% to 15.9%, respectively. In general, the intermetallics improved the strength of the alloy but reduced the toughness; therefore, the elongation decreased because of the presence of the Gd intermetallics.

Table 2. Tensile properties of the experimental alloys and borated stainless steel.

	UTS (MPa)	YS (MPa)	E (%)
304	534.2 ± 24.7	217.5 ± 7.4	69.3 ± 1.7
316	455.4 ± 16.3	210.0 ± 8.6	63.4 ± 2.7
5A	734.7 ± 10.1	576.1 ± 10.3	30.9 ± 2.6
304-Gd	572.6 ± 67.3	225.4 ± 6.8	38.3 ± 3.3
316-Gd	504.0 ± 15.6	220.9 ± 5.1	49.4 ± 4.6
5A-Gd	776.5 ± 24.3	622.4 ± 4.9	15.9 ± 5.1
304B6 (1.6 wt.% B)	515	205	9–20
304B7 (2 wt.% B)	515	205	6–17

Borated stainless steel, which is a representative thermal neutron absorber listed in ASTM standard A887, is made by adding B content ranging from 0.2 wt.% to a maximum of 2.25 wt.% to 304 (austenitic stainless steel). ASTM standard A887 has minimum mechanical property requirements according to the B content for use as a thermal neutron absorber. The results of the experimental alloys (304-Gd, 316-Gd, and 5A-Gd) were compared with the minimum mechanical property requirements of the ASTM standard [26–28]. Table 2 shows the tensile test results of the experimental alloys and the mechanical property requirements for 304B6 and 304B7 alloys with B contents of 1.6 and 2 wt.%, respectively. Generally, as the B content in the alloy increased, grain boundary segregation occurred and B intermetallics were nonuniformly dispersed. Therefore, as the amount of added B increased, the elongation decreased significantly. In the case of 304B7, in which the amount of B added was similar to the Gd amount of the experimental alloys, the required values of the ultimate tensile strength, yield strength, and elongation were 515 MPa, 205 MPa, and ~6–17%, respectively. The 304-Gd showed relatively high values for all three properties, with 316-Gd and 5A-Gd also exceeding the standard.

Figure 5 and Table 3 show the Charpy impact test results of the experimental alloys with solution heat treatment. 304, 316, and 5A showed impact energies of 125, 145, and 144 J, respectively, before Gd was added. In the case of 304-Gd (after adding Gd), the impact energy was reduced by approximately 49% to 64 J. The impact energy of 316-Gd decreased by approximately 56% to 62 J and 5A-Gd also showed a value of 77 J, which was approximately 46% lower than that before the Gd addition. The ASTM standard requires an impact energy of 22 J for 304B6, with 1.6 wt.% B added, and 14 J for 304B7, with 2 wt.% B added, as minimum values [28,29]. In the case of 304-Gd, which is an experimental alloy with a composition most similar to 304B7, the impact energy was 64 J, which is approximately 2.9 times higher than that of 304B7. Our findings align closely with prior research indicating that tensile properties, including ultimate tensile strength and strain at the point of fracture, exhibit a decline with increasing Gd content in the alloys. Qi et al. proposed that the proliferation of Gd-based intermetallic compounds significantly increases the interface between the second phase and the matrix [8]. This, in turn, results in a diminished bonding strength at this interface, rendering the material susceptible to crack initiation and propagation under tensile loads, ultimately leading to material fracture. Conversely, Wan et al. confirmed that an excessive accumulation of Gd-based intermetallics can trigger cracking during tensile testing [30]. This underscores the trade-off between augmenting neutron absorption capacity through increased Gd-based intermetallic content and impeding matrix connectivity, which, in turn, reduces material ductility.

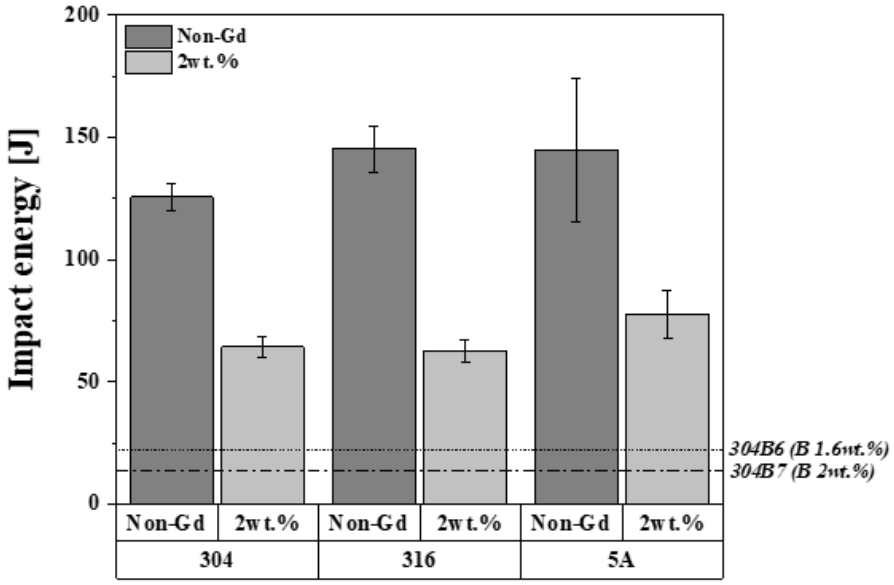

Figure 5. Changes in Charpy impact energy of the experimental alloys with the addition of Gd.

Table 3. Charpy impact energy of the experimental alloys and borated stainless steel.

Alloys	Impact Energy (J)
304	125.6 ± 5.1
316	145.4 ± 9.3
5A	144.8 ± 26.1
304-Gd	64.3 ± 3.8
316-Gd	62.8 ± 4.9
5A-Gd	77.7 ± 9.7
304B6 (1.6 wt.% B)	22
304B7 (2 wt.% B)	14

SEM fractographs of the experimental alloys after Charpy impact tests are shown in Figures 6–8. Figure 6 is the result of a low-magnification observation of the fracture surface. In the cases of Figure 6a–c, before the addition of Gd, ductile failure was observed. Conversely, ductile failure was observed after Gd was added, but cleavage failure was observed in some areas. Figure 7 shows images of the fracture surface observed at high magnification. In the cases of Figure 7a–c, before adding Gd, the sizes of the dimples were generally uniform, and the insides of the dimples were clean. Even after Gd was added, some brittle fractures were observed, but the dimples were evenly distributed overall, indicating a ductile fracture. However, Gd intermetallics were present inside the dimple and showed a broken shape. In general, precipitates or inclusions cause stress concentration and act as the main cause of lower shock energy absorption. In previous research, adding Gd in a small amount improved the impact properties by changing the inclusion morphology. However, in the experimental alloys in this study, stress was concentrated on the Gd intermetallics, and thus, it is thought that the dimple did not grow large and deep. The Gd intermetallics at the center of the dimple were analyzed using SEM-EDS, and the results are shown in Figure 8. The size and fracture patterns of the Gd intermetallics varied, with most of the chemical compositions being Fe–Cr–Ni–Gd-based intermetallics.

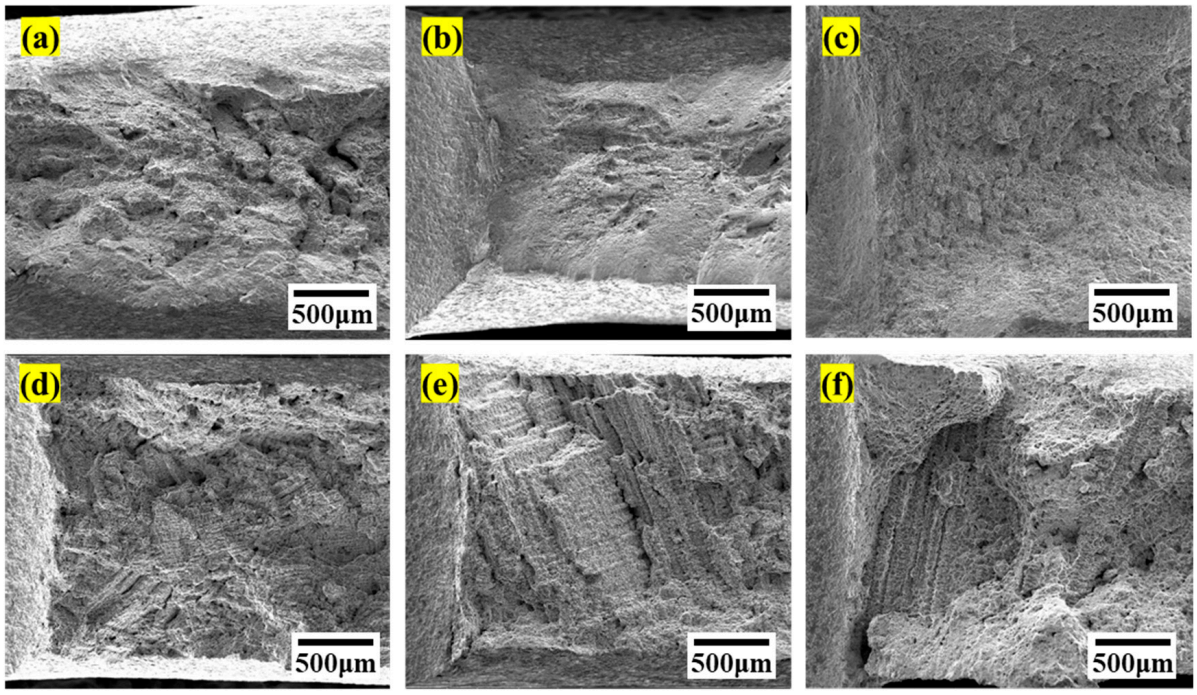

Figure 6. Low-magnification SEM images of the fracture surface of the experimental alloys: (**a**) 304, (**b**) 316, (**c**) 5A, (**d**) 304-Gd, (**e**) 316-Gd, and (**f**) 5A-Gd.

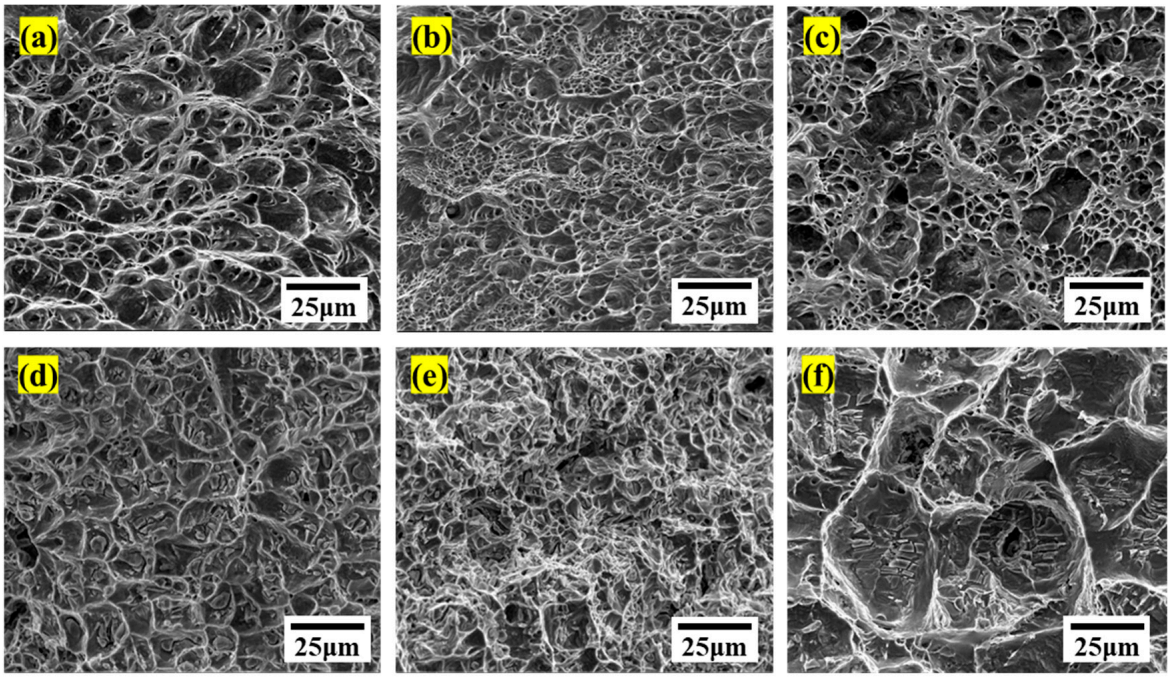

Figure 7. High-magnification SEM images of the fracture surface of the experimental alloys: (**a**) 304, (**b**) 316, (**c**) 5A, (**d**) 304-Gd, (**e**) 316-Gd, and (**f**) 5A-Gd.

3.3. Corrosion Resistances of the Alloys

Figure 9 and Table 4 show potentiodynamic polarization test results for the experimental alloys in an artificial seawater solution. After Gd was added, the polarization curves of all alloys showed a decrease in corrosion potential (E_{corr}) and an increase in corrosion current density (I_{corr}) compared with those of the alloys without the Gd addition. In general, the corrosion resistance increased as the E_{corr} value increased and the I_{corr} value

decreased. In the case of the experimental alloy, the corrosion resistance decreased after adding Gd. However, as can be seen from the results in Table 4, the properties slightly decreased compared with those before the addition of Gd. In the case of 304, the R_p values were 107.17 and 33.206 before and after the Gd addition, respectively. In the cases of 316 and 5A, the R_p values were 133.12 and 35.391 and 119.69 and 17.02 before and after the Gd addition, respectively. The decreases in Rp value after the Gd addition were 69.01%, 74.41%, and 85.78% for 304, 316, and 5A, respectively. It is noteworthy that our results are similar to previous studies in that the corrosion properties of the Gd-incorporated alloys decreased as the contents of Gd increased [8,17,31]. This was attributed to the higher reactivity of Gd compared with Fe, Cr, and Ni. In the primary cell, Gd tended to dissolve at the negative electrode, leading to preferential corrosion of Gd-based intermetallic compounds. Additionally, the tendency of these Gd-based compounds to corrode more readily stemmed from Gd's heightened electrochemical activity relative to other matrix elements and its limited capacity to create protective passive films.

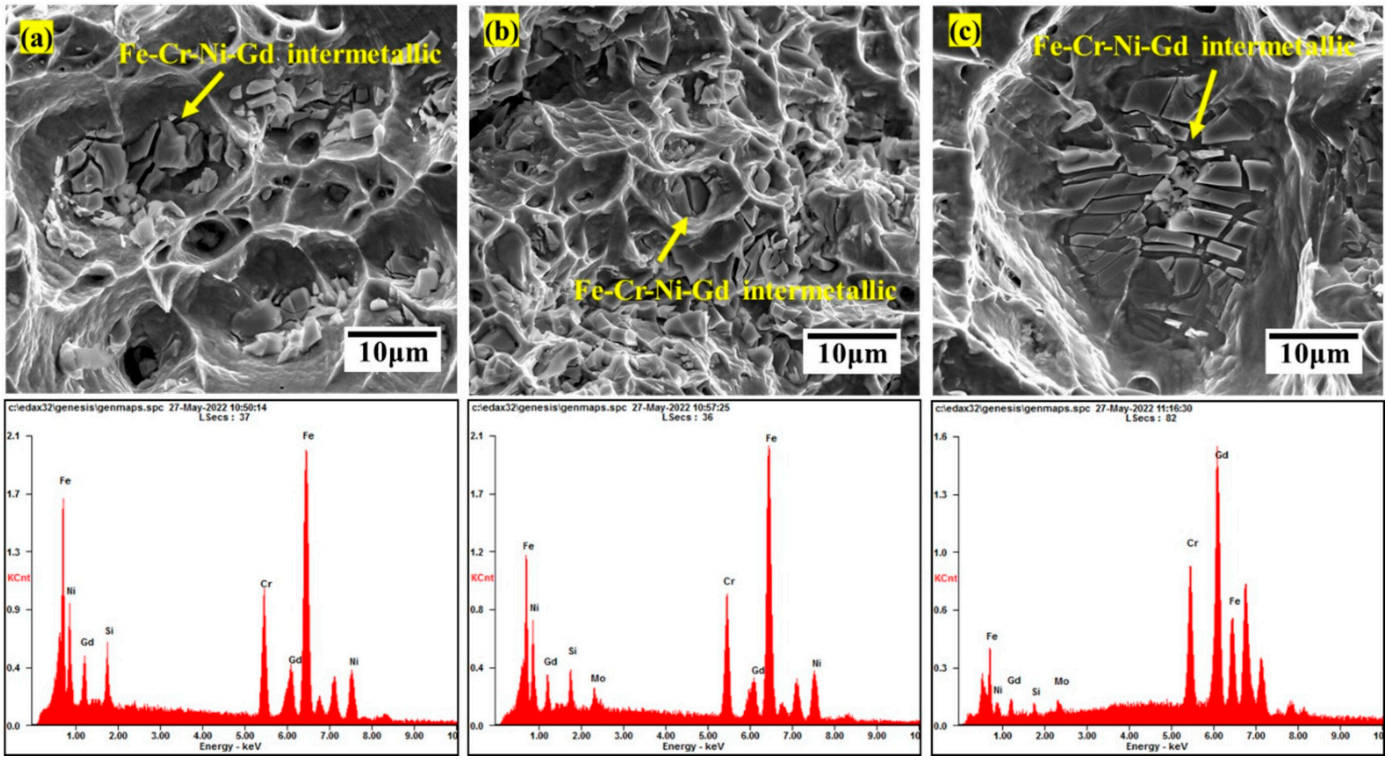

Figure 8. SEM images (**top**) of fracture surfaces and EDS analysis results (**bottom**) for the experimental alloys: (**a**) 304-Gd, (**b**) 316-Gd, and (**c**) 5A-Gd.

Table 4. Potentiodynamic polarization parameters of the experimental alloys.

Alloys	E_{corr} (mV vs. Ag/AgCl)	I_{corr} (μA/cm^2)	β_c (mV/decade)	β_a (mV/decade)	R_p (kΩ·cm^2)
304	−229.1	0.55	328.1	233.9	107.2
316	−180.6	0.19	128.8	109.9	133.1
5A	−220.1	0.38	145.6	375.5	119.7
304-Gd	−318.4	1.35	313.0	153.1	33.2
316-Gd	−299.1	2.68	387.5	501.0	35.4
5A-Gd	−245.8	4.84	498.4	305.8	17.0

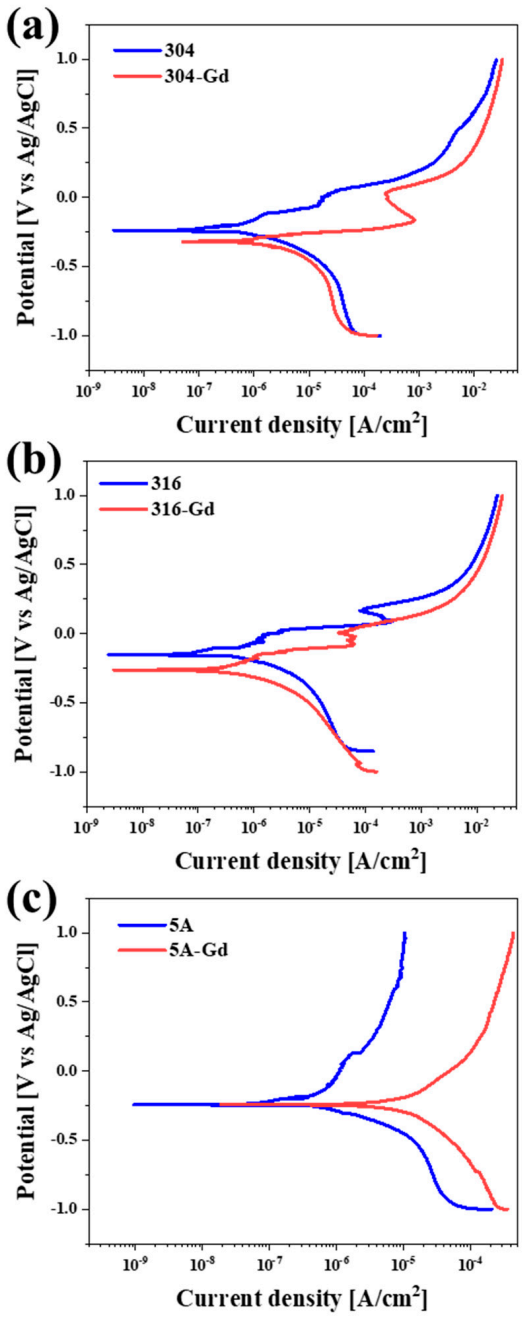

Figure 9. Potentiodynamic polarization curves for (**a**) 304 and 304-Gd, (**b**) 316 and 316-Gd, and (**c**) 5A and 5A-Gd in artificial seawater.

3.4. Thermal-Neutron-Absorbing Properties of the Alloys

Theoretical calculations of thermal neutron absorption in the fabricated alloys were conducted utilizing the Beer–Lambert Law. In Figure 10, we present the correlation between the thermal neutron transmission ratio (I/I_0) and varying Gd concentrations in fabricated steel alloys with different thicknesses of alloys. All the graphs exhibit a consistent pattern characterized by an exponential reduction in the neutron transmission ratio with increasing Gd concentrations in the steel-alloy-based thermal-neutron-absorbing material. Furthermore, with a thicker fabricated steel alloy, the thermal neutron transmission ratio decreased. Consequently, when the content of Gd in alloys was 2 wt%, nearly all neutrons were effectively shielded.

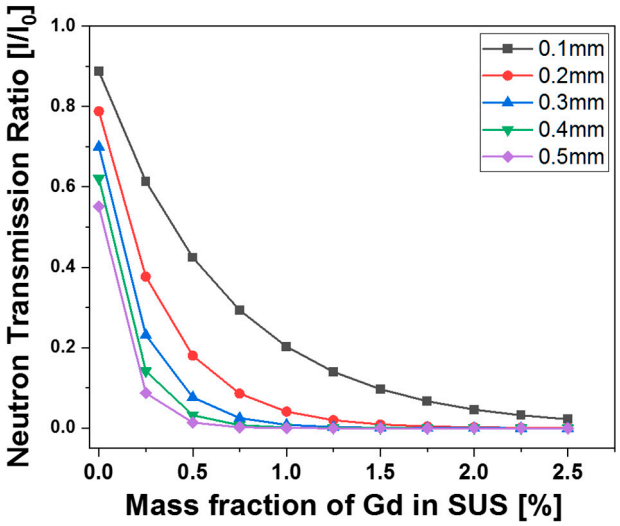

Figure 10. The relationship between the neutron transmission ratio and contents of Gd in various steels.

In our previous paper, the thermal neutron transmission ratio of the Fe alloy with 1 wt% of Gd was found to be similar to that of the Al composite with 30 vol% of boron carbide (B_4C), which is extensively researched as a thermal-neutron-absorbing and -shielding material [1]. It is important to highlight that even a small amount of Gd can effectively absorb thermal neutrons. Moreover, as shown in Figure 10, we observed that the neutron transmission ratio exponentially decreased with the increase in the thickness of the fabricated alloys and the Gd content in steel. It is widely recognized that the uniform distribution of nano-sized dispersoids within the matrix, which serve as anchoring points for dislocations and repositories for irradiation-induced defects, can notably enhance both the elevated mechanical properties and radiation resistance of alloys [18]. Consequently, the simultaneous improvement of mechanical properties and thermal-neutron-shielding performance of the alloy appears promising and was achieved through the uniform dispersion of Gd-based intermetallics in the matrix. Although the mechanical properties and corrosion resistance decreased in all conditions due to the strong oxidizing nature of Gd, which led to the formation of numerous Gd-based oxides, the results were still higher than those of commercial borated steel. These outcomes suggest that steel alloys with 2 wt% Gd show immense potential as thermal-neutron-absorbing or -shielding materials that are capable of surpassing the constraints faced by current thermal-neutron-absorbing and -shielding structural materials.

In recent years, rare earth elements have gained prominence in the realm of thermal neutron absorption due to their substantial neutron absorption cross-section. Notably, certain rare earth elements, exemplified by Gd, exhibit a notably higher thermal neutron absorption cross-section compared with boron. Consequently, these elements have evolved into pivotal constituents of shielding materials [32,33]. It becomes evident that an ideal formulation for thermal-neutron-shielding materials should encompass a combination of both base metals, such as Fe-based alloys and Al-based alloys, and heavy rare earth elements. These rare earth particles possess a distinctive capability to absorb low-energy neutrons and operate in concert to moderate higher-energy neutrons through inelastic scattering [34].

Enhancing the efficient utilization of rare earth elements and optimizing the design of shielding capabilities is imperative. This strategic approach serves as a foundational cornerstone for advancing the overall performance of materials, encompassing attributes like mechanical properties, functionalization, and heightened shielding efficacy. In this study, we used Gd as a thermal-neutron-shielding and -absorbing material, but it is possible to create materials with thermal-neutron-shielding ability using other rare earth metals as well. We plan to conduct further research on this. Additionally, enhancing the efficient

utilization of rare earth elements and optimizing the design of shielding capabilities is imperative. This strategic approach serves as a foundational cornerstone for advancing the overall performance of materials, encompassing attributes like lightweight properties, functionalization, and heightened shielding efficacy.

4. Conclusions

In this study, Gd was added to commercial 304 and 316 austenitic and DSS 5A alloys to confirm its potential as a next-generation neutron absorber. The experimental alloys were manufactured using VAM, and 2 wt.% of Gd was added to 304, 316, and 5A commercial alloys. After a solution heat treatment, the microstructure, mechanical properties, and corrosion resistance were evaluated. The mechanical property evaluation results were compared with the minimum physical property requirements for borated stainless steel in ASTM standard A887. As a result of the microstructure observation, Gd was found to be uniformly distributed in the alloy as intermetallics. There was no segregation or clustering, and there were no coarse intermetallics. The Gd intermetallic peak was also not observed via XRD analysis. The tensile test results show that the ultimate tensile strength and yield strength increased by up to 11% after the addition of Gd. Although the elongation decreased by up to 48%, a significantly higher elongation value was observed compared with that of borated stainless steel. The Charpy impact test also showed a decrease in impact energy by up to 56% after the addition of Gd, but the impact energy was twice as high as that of borated stainless steel. As a result of analyzing the SEM fractographs, it was confirmed that brittle fracturing occurred in some areas after the Gd was added. Additionally, Gd intermetallics were present inside the dimple and showed a broken shape. Potentiodynamic polarization tests of the experimental alloys were performed, and the corrosion resistance deteriorated after Gd was added. The Rp values decreased by 69.01%, 74.41%, and 85.78% for 304, 316, and 5A, respectively, after Gd was added. The mechanical properties of the experimental alloys were confirmed to be superior to those of borated stainless steel and the neutron absorption capacity was also confirmed to be superior to that of the additive element.

Supplementary Materials: The following supporting information can be downloaded from https://www.mdpi.com/article/10.3390/met14010016/s1—Table S1: Neutron absorbing cross-sections of Fe and Gd.

Author Contributions: S.O., H.-D.J., R.J. and H.-J.K.; methodology, S.O., J.-H.A., D.H.C. and Y.C.; validation, J.-H.A. and H.-D.J.; investigation, R.J., H.-J.K. and Y.C.; data curation, R.J., H.-J.K. and Y.C.; formal analysis, S.O., H.L. and H.-D.J.; writing—original draft preparation, S.O. and H.L.; supervision, D.H.C. and H.-D.J.; project administration, Y.C. and H.-D.J.; funding acquisition. All authors have read and agreed to the published version of the manuscript.

Funding: This work was supported by The Catholic University of Korea, Research Fund, 2022; the National Research Foundation of Korea (NRF) grant funded by the Korean government (MSIT) (no. 2021R1A2C1091301); and the Technology Innovation program managed by the Ministry of Science and ICT and the Ministry of Trade, Industry, and Energy (MOTIE) (nos. 20010488 and 20019192).

Data Availability Statement: The data presented in this study are available on request from the corresponding author. The data are not publicly available due to privacy.

Conflicts of Interest: Author Younghwan Chu was employed by the company Fospia Co., Ltd.; Author Dae Hyun Choi was employed by the company SHINWOO CNC KOREA Co., LTD. The remaining authors declare that the research was conducted in the absence of any commercial or financial relationships that could be construed as a potential conflict of interest.

References

1. Lee, S.-W.; Ahn, J.-H.; Moon, B.-M.; Kim, D.; Oh, S.; Kim, Y.-J.; Jung, H.-D. Preliminary study on FeGd alloys as binary alloys and master alloys for potential spent nuclear fuel (SNF) application. *Mater. Des.* **2020**, *194*, 108906. [CrossRef]
2. Moon, B.-M.; Lee, S.-W.; Kim, M.-J.; Jung, S.-R.; Kim, Y.-J.; Jung, H.-D. The effect of gadolinium on the microstructures and Charpy impact properties of super duplex stainless steels. *Metals* **2018**, *8*, 474. [CrossRef]

3. Taylor, R.; Mathers, G.; Banford, A. The development of future options for aqueous recycling of spent nuclear fuels. *Prog. Nucl. Energy* **2023**, *164*, 104837. [CrossRef]
4. Qi, Z.; Yang, Z.; Li, J.; Guo, Y.; Yang, G.; Yu, Y.; Zhang, J. The advancement of neutron-shielding materials for the transportation and storage of spent nuclear fuel. *Materials* **2022**, *15*, 3255. [CrossRef] [PubMed]
5. Karley, D.; Shukla, S.K.; Rao, T.S. Microbiological assessment of spent nuclear fuel pools: An in-perspective review. *J. Environ. Chem. Eng.* **2022**, *10*, 108050. [CrossRef]
6. Holdsworth, A.F.; Eccles, H.; Sharrad, C.A.; George, K. Spent Nuclear Fuel—Waste or Resource? The Potential of Strategic Materials Recovery during Recycle for Sustainability and Advanced Waste Management. *Waste* **2023**, *1*, 249–263. [CrossRef]
7. Gan, B.; Liu, S.; He, Z.; Chen, F.; Niu, H.; Cheng, J.; Tan, B.; Yu, B. Research progress of metal-based shielding materials for neutron and gamma rays. *Acta Metall. Sin. (Engl. Lett.)* **2021**, *34*, 1609–1617. [CrossRef]
8. Qi, Z.-D.; Yang, Z.; Yang, X.-G.; Wang, L.-Y.; Li, C.-Y.; Dai, Y. Performance study and optimal design of Gd/316L neutron absorbing material for Spent Nuclear Fuel transportation and storage. *Mater. Today Commun.* **2023**, *34*, 105342. [CrossRef]
9. Jung, Y.; Lee, M.; Kim, K.; Ahn, S. 10B (n, α) 7Li reaction-induced gas bubble formation in Al–B4C neutron absorber irradiated in spent nuclear fuel pool. *J. Nucl. Mater.* **2020**, *533*, 152077. [CrossRef]
10. Jiang, L.; Xu, Z.; Fei, Y.; Zhang, Q.; Qiao, J.; Wu, G. The design of novel neutron shielding (Gd + B4C)/6061Al composites and its properties after hot rolling. *Compos. Part B Eng.* **2019**, *168*, 183–194. [CrossRef]
11. Kim, M.J.; Kim, W.; Lee, D.; Lemaire, M.; Lee, H.-J.; Sohn, D.-S.; Kwon, H. Development of integral type spent fuel pool storage rack with gadolinium and europium-containing structure materials. *Ann. Nucl. Energy* **2019**, *130*, 107–117. [CrossRef]
12. Hur, D.H.; Jeon, S.-H.; Han, J.; Park, S.-Y.; Chun, Y.-B. Effect of gadolinium addition on the corrosion behavior and oxide properties of titanium in boric acid solution at 50 °C. *J. Mater. Res. Technol.* **2022**, *21*, 3051–3061. [CrossRef]
13. Xu, Z.; Jiang, L.; Zhang, Q.; Qiao, J.; Gong, D.; Wu, G. The design of a novel neutron shielding B4C/Al composite containing Gd. *Mater. Des.* **2016**, *111*, 375–381. [CrossRef]
14. Cong, S.; Ran, G.; Li, Y.; Chen, Y. Ball-milling properties and sintering behavior of Al-based Gd2O3–W shielding materials used in spent-fuel storage. *Powder Technol.* **2020**, *369*, 127–136. [CrossRef]
15. Lister, T.; Mizia, R.; Pinhero, P.; Trowbridge, T.; Delezene-Briggs, K. Studies of the corrosion properties of Ni-Cr-Mo-Gd neutron-absorbing alloys. *Corrosion* **2005**, *61*, 706–717. [CrossRef]
16. Mizia, R.E.; Lister, T.E.; Pinhero, P.J.; Trowbridge, T.L.; Hurt, W.L.; Robino, C.V.; Stephens, J.J., Jr.; DuPont, J.N. Development and testing of an advanced neutron-absorbing gadolinium alloy for spent nuclear fuel storage. *Nucl. Technol.* **2006**, *155*, 133–148. [CrossRef]
17. Wang, W.; Zhang, J.; Wan, S.; Zhang, T. Design, fabrication and comprehensive properties of the novel thermal neutron shielding Gd/316L composites. *Fusion Eng. Des.* **2021**, *171*, 112566. [CrossRef]
18. Yang, X.; Song, L.; Chang, B.; Yang, Q.; Mao, X.; Huang, Q. Development of Gd-Si-O dispersed 316L stainless steel for improving neutron shielding performance. *Nucl. Mater. Energy* **2020**, *23*, 100739. [CrossRef]
19. Wang, H.; Wang, T.; Peng, J. Effect of gadolinium addition on microstructure, mechanical properties and corrosion resistance of 316L austenitic stainless steels. *Phys. Met. Metallogr.* **2021**, *122*, 1640–1647. [CrossRef]
20. Baik, Y.; Choi, Y.; Moon, B.M.; Sohn, D.S.; Bogdanov, S.G.; Pirogov, A.N. Effect of gadolinium addition on the corrosion, wear, and neutron absorbing behaviors of duplex stainless steel sheet. *Phys. Met. Metallogr.* **2015**, *116*, 1135–1142. [CrossRef]
21. Ahn, J.-H.; Jung, H.-D.; Im, J.-H.; Jung, K.H.; Moon, B.-M. Influence of the addition of gadolinium on the microstructure and mechanical properties of duplex stainless steel. *Mater. Sci. Eng. A* **2016**, *658*, 255–262. [CrossRef]
22. Jung, M.Y.; Baik, Y.; Choi, Y.; Sohn, D.-S. Corrosion and mechanical properties of hot-rolled 0.5% Gd-0.8% B-stainless steels in a simulated nuclear waste treatment solution. *Nucl. Eng. Technol.* **2019**, *51*, 207–213. [CrossRef]
23. Schmidt, M.; Del Corso, G.; Klankowski, K.; Lherbier, L.; Novotnak, D. Review of the Development and Testing of a New Family of Boron and Gadolinium-bearing Dual Thermal Neutron Absorbing Alloys-13026. In Proceedings of the WM2013: Waste Management Conference: International Collaboration and Continuous Improvement, Phoenix, AZ, USA, 24–28 February 2013; pp. 24–28.
24. Saeed, A. Developed borated austenitic stainless steel alloys as nuclear reactor control rods. *Nucl. Eng. Des.* **2023**, *413*, 112515. [CrossRef]
25. Kang, M.-H.; Cheon, K.-H.; Jo, K.-I.; Ahn, J.-H.; Kim, H.-E.; Jung, H.-D.; Jang, T.-S. An asymmetric surface coating strategy for improved corrosion resistance and vascular compatibility of magnesium alloy stents. *Mater. Des.* **2020**, *196*, 109182. [CrossRef]
26. Lister, T.; Mizia, R.E.; Erickson, A.; Matteson, B. General and Localized Corrosion of Borated Stainless Steels. In Proceedings of the NACE CORROSION, New Orleans, LA, USA, 16–20 March 2008; p. NACE-08590.
27. Lister, T.; Mizia, R.; Erickson, A.; Trowbridge, T. *Electrochemical Corrosion Testing of Neutron Absorber Materials*; Idaho National Lab. (INL): Idaho Falls, ID, USA, 2007.
28. Robino, C.; Cieslak, M. High-temperature metallurgy of advanced borated stainless steels. *Metall. Mater. Trans. A* **1995**, *26*, 1673–1685. [CrossRef]
29. He, J. *The Effect of Boron Content, Temperature, and Neutron Fluence on the Mechanical Properties of the Modified Type 304 Stainless Steels with Boron*; The Pennsylvania State University: State College, PA, USA, 1995.
30. Wan, S.; Wang, W.; Chen, H.; Zhou, J.; Zhang, Y.; Liu, R.; Feng, R. 155/157Gd areal density: A model for design and fabrication of Gd2O3/316L novel neutron shielding composites. *Vacuum* **2020**, *176*, 109304. [CrossRef]

31. Ha, H.-Y.; Lee, T.-H.; Jo, H.-H.; Lee, J.; Jang, J.H. Corrosion behavior of (Fe, Ni)–Gd intermetallic compounds in FeNi-based neutron-absorbing steels. *J. Nucl. Mater.* **2023**, *578*, 154367. [CrossRef]
32. Florez, R.; Loaiza, A.; Giraldo, C.H.C.; Colorado, H.A. Calcium silicate phosphate cement with samarium oxide additions for neutron shielding applications in nuclear industry. *Prog. Nucl. Energy* **2021**, *133*, 103650. [CrossRef]
33. Castley, D.; Goodwin, C.; Liu, J. Computational and experimental comparison of boron carbide, gadolinium oxide, samarium oxide, and graphene platelets as additives for a neutron shield. *Radiat. Phys. Chem.* **2019**, *165*, 108435. [CrossRef]
34. Jing, H.; Geng, L.; Qiu, S.; Zou, H.; Liang, M.; Deng, D. Research progress of rare earth composite shielding materials. *J. Rare Earths* **2023**, *41*, 32–41. [CrossRef]